The 2016 World Congress on
Advances in Civil, Environmental, and Materials Research (ACEM16)
Jeju Island, Korea, August 28-September 1, 2016

Study on Numerical Simulation and Mechanism of Soft Flutter of a Bridge Deck

*Xuyong Ying [1)], Fuyou Xu [2)] and Zhe Zhang[3)]

[1), 2), 3)] *School of Civil Engineering, Dalian University of Technology, China*
[1)] *yingxuyong@hotmail.com*

ABSTRACT

Based on *ANSYS FLUENT*, a fluid-structure interaction (FSI) model has been developed to investigate the soft flutter characteristics of a bridge deck. Its accuracy is verified by simulating the critical flutter state of one thin plate section with theoretical solutions. The unsteady flows around a elastically supported deck at different wind speeds and initial angles of attack are simulated. The soft flutter phenomenon of the bridge deck is well captured by the present numerical model. The simulated results indicate that the soft flutter amplitude increases gradually with the wind speed until the hard flutter occurs. The soft flutter of bridge deck is in a bending-torsion coupled mode, and the coupled vibration frequency decreases with the increase of wind speed. The motion induced vortex (MIV) generated and shed periodically on the deck surface is the fundamental cause of the soft flutter of bridge deck. The time-varying energy input from the fluid is also investigated to unveil the mechanism of soft flutter. There must exist an aerodynamic energy balance for bridge deck during soft flutter, i.e., the fluid-structure system absorbs and dissipates energy in a certain vibration region so as to achieve the balance.

1. INTRODUCTION

Flutter analysis is classically based on Scanlan's linear self-excited forces model (Scanlan and Tomko, 1971), in which consider that the bridge deck undergoes harmonic vibration with net zero damping at critical flutter state. This kind of flutter is classified as the hard type, and further increase of wind speed will result in catastrophic divergent vibration. According to the Scanlan's model, the self-excited forces are the linear functions of deck motions and flutter derivatives. Actually, the self-excited forces inevitably contain nonlinear components due to the bluff configurations and large amplitudes, and therefore, nonlinear aeroelastic phenomenon may occur for some cases of bridge flutter. Chen et al. (2005) investigated the characteristics of the

---

[1)] Graduate Student
[2)] Associate Professor
[3)] Professor

aerodynamic forces acting on bridge section by using forced vibration tests in wind tunnel. Results indicated that the self-excited aerodynamic forces of bluff section were nonlinear and contained noticeable higher order harmonics, even when the deck section experiences sinusoidal vibrations with small amplitudes. For bluff deck sections or in the condition of large initial angle of attack (Xu and Chen, 2009; Long, 2010; Zhu and Gao, 2015), a large number of wind tunnel tests found that when the wind speed is sufficiently high, the decks experience limit cycle oscillations (LCO), rather than the divergent hard-type flutter. This kind of LCO can be classified as the soft-type flutter, in which the deck reaches steady-state vibration for a specific wind speed. Zhang (2007) presented a single-degree-of-freedom (SDOF) nonlinear aerodynamic model, by which the phenomenon of soft flutter was satisfactorily explained. Zhu and Gao (2015) carried out a series of bridge deck section model tests to investigate the soft flutter of typical sections. The results showed that the deck soft flutter is the coupled vertical and torsional oscillation with a single frequency.

The similar aeroelastic phenomenon can be observed in the field of aeronautics and astronautics engineering, e.g., in a wide variety of aircraft during flight (Cunningham, 2003), in wind tunnel tests (Majid and Basri, 2008; Amandolese et al., 2013), and in numerical simulations (Tang et al., 2003; Wang et al., 2011). In recent years, the performance of LCO for aircraft wings has been well studied. However, the soft flutter phenomenon for bridge decks sections has received less attention. The intensive investigation of soft flutter phenomenon has important significance to construct more accurate bridge flutter theory and judging criterion for flutter stability.

In present paper, aerodynamic energy analysis for a bridge deck during soft flutter is conducted using the numerical simulation approach. Section 2 presents the fluid-structure interaction (FSI) model and solving strategy. Section 3 describes the structural parameter and geometry of the deck section used in present study. In section 4, the critical flutter state of a thin plate section is simulated in order to validate the accuracy of the present numerical model; the soft flutter response of bridge deck for various wind speeds and initial angles of attack is then analyzed. The preliminary discussion of soft flutter mechanism using aerodynamic energy analysis is conducted in Section 5.

2. NUMERICAL MODEL DESCRIPTION

2.1 Governing equations for fluid

The incompressible, unsteady, 2-D air flow with moving boundaries can be modeled by means of the Reynolds Averaged Navier-Stokes (RANS) equations. For the numerical aeroelastic simulation that contains dynamic meshes, an important requirement is the accurate simulation for the interactions between air flow and moving deck section. In the present study, the governing equations are given in Arbitrary Lagrange-Euler (ALE) formulation, which accommodates the moving boundaries and any subsequent deformation of the underlying discrete mesh. By introducing the grid velocity u_{mj} of the moving mesh, the ALE formulation for mass and momentum of incompressible fluid may be expressed as

$$\frac{\partial \rho}{\partial t} + \frac{\partial \rho (u_j - u_{mj})}{\partial x_j} = 0 \text{ , (1a)}$$

$$\frac{\partial \rho u_i}{\partial t} + \frac{\partial \rho (u_j - u_{mj}) u_i}{\partial x_j} = -\frac{\partial p}{\partial x_i} + \frac{\partial}{\partial x_j}(\mu_{eff} \frac{\partial u_i}{\partial x_j}) + S_i \text{ , (1b)}$$

where u_i or u_j, ρ, x_j and p are the fluid velocity components, the fluid density, the Cartesian spatial coordinates and the fluid pressure, respectively; S_i denotes the additional momentum source contributions, if any; μ_{eff} is the effective viscosity which includes laminar and turbulent contributions (Hassan et al., 2010). In the RANS approach, the turbulence viscosity is modeled by the SST $k-\omega$ model (Menter, 1994). Ying et al. (2012) conducted a comprehensive simulation of unsteady flow around rectangular cylinders by using different RANS approaches, and the SST $k-\omega$ model is found to be the best choice among various RANS models and has accuracy enough to be suitable for practical problems. Further details on the SST turbulence model implementation may be referred to Menter (1994).

The *ANSYS FLUENT* adopted in this study uses the finite-volume method (FVM) to solve the fluid governing equations. The ALE formulation of governing equation enables the conservative fluid calculations with mesh adaptation in time. The discretization method of governing RANS equations remains unchanged from the general application of FVM (Schneider et al., 1987). The second order implicit scheme and upwind scheme are used for the time and spatial discretization, respectively. SIMPLE (semi-implicit pressure linked equations) algorithm is used for solving the discretized governing equations. The time-step is set as Δt=0.001*s*.

2.2 Computational Domain and Mesh Arrangement

The computational domain and boundary conditions are schematically shown in Fig. 1 for a two dimensional *x-y* slice. Due to large vibration amplitudes may be concerned, the wide rectangular computational domain is set as 16.0×5.0 m. The boundaries are sufficiently far away from the sections so as to eliminate the flow obstacle effect on the inflow and outflow boundary conditions. At the inflow boundary, the flow with a low turbulence intensity of 0.5% is used. A non-slip condition is used for the section surfaces and the top and bottom surface of the domain. It is assumed that the flow is fully developed at the outlet boundary.

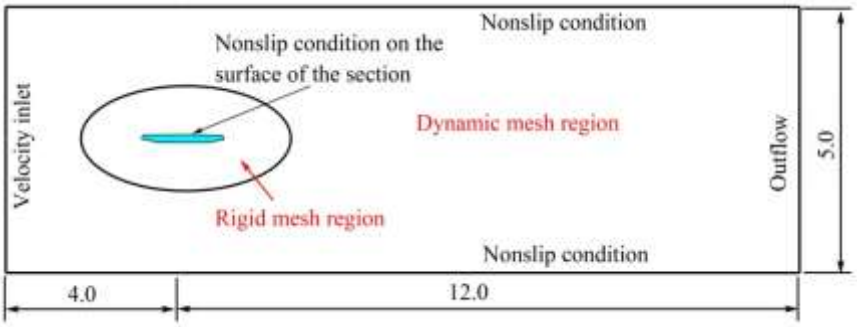

Fig. 1 Computational domain and boundary conditions (unit: m).

Considering the mesh number should be as low as possible to obtain high efficiency in computation, the hybrid grids are used for the whole computational domain. The structured quadrangular grid is generated for the zone in the vicinity of deck section, while the unstructured triangular grid is adopted for the outside zone. The height of 0.0001 *m* is selected for the first layer close to deck surface and the total number of mesh cells is 86136, which is adequate to resolve the velocity and viscous sublayer. A view of meshes near the surface of the deck section is depicted in Fig. 2.

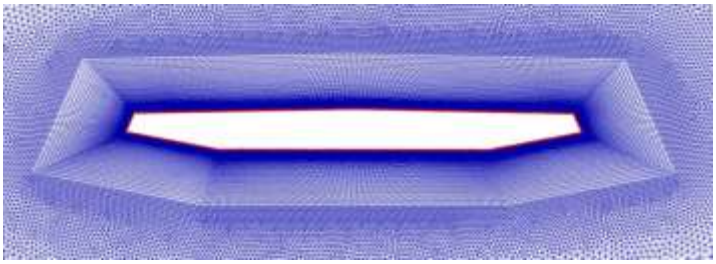

Fig. 2 Mesh near the surface the deck section

For fluid-structure interaction (FSI) problems, the section model is subjected to heaving and/or torsional vibration, and the dynamic mesh technique is employed to fulfill this target. The present whole computational domain is decomposed into two sub-domains those similar to the early work by Fransos and Bruno (2006), as shown in Fig. 1. The inner oval-shaped region is rigidly connected with the sectional model and move synchronously, while the mesh in outer region deforms at each iteration time-step. The spring-based smoothing technique is adopted to accommodate the deformation of dynamic mesh. Not any deformation occurs for the rigid mesh region and their quality remains unchanged throughout the whole calculation process, which is a benefit especially for solving the viscous sub-layer that close to the section surface. The more detailed descriptions for dynamic mesh technique may be found in Xu et. al. (2014).

2.3 Governing equations for bridge deck

For a 2-D rigid section, its planar vibrations can be described in terms of three displacement components, i.e., *p*, *h* and *α,* defined at the shear center (Nomura and Hughes, 1992). *p* and *h* are the translational motion displacement in the *x* and *y* directions as shown in Fig. 3, respectively, and *α* is the torsional displacement about the shear center. The aeroelastic drag force, lift force, and twist moment induced by

lateral motion have been generally regarded as insignificant to bridge flutter. Thus, a typical 2-D section model with 2-DOF, i.e., *h* and *α*, is used in the formulation of present aeroelastic simulation. The torsional displacement *α* is taken positive clockwise.

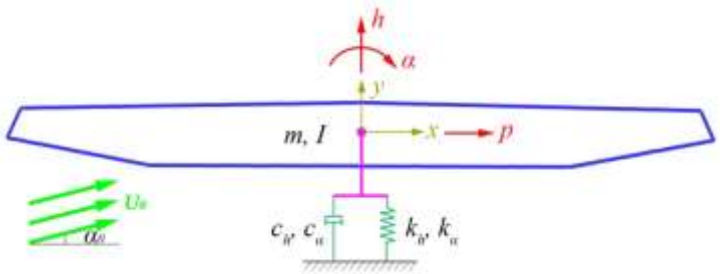

Fig. 3 Structural reference system

The deck model is assigned mass (*m*, *I*), stiffness (k_h, k_α) and viscous damping coefficients (c_h, c_α), and the motion equations for the section model can be expressed as

$$m\ddot{h}(t)+c_h\dot{h}(t)+k_h h(t)=F_L(t)\text{, (2a)}$$

$$I\ddot{\alpha}(t)+c_\alpha\dot{\alpha}(t)+k_\alpha\alpha(t)=M_T(t)\text{, (2b)}$$

where $\ddot{h}(t)$, $\dot{h}(t)$, $h(t)$ are the vertical acceleration, velocity, and displacement, respectively; $\ddot{\alpha}(t)$, $\dot{\alpha}(t)$, $\alpha(t)$ are the torsional acceleration, velocity, and displacement, respectively; $F_L(t)$ and $M_T(t)$ are the aerodynamic lift and twist moment acting on the section model, respectively. The fourth-order Runge-Kutta method is used to discretely solve the structural motion Eq. (2). For the vertical motion, the vertical motion Eq. (2a) can be expressed as a first order differential equation:

$$f(\dot{h},h)=F_L(t)/m-2\xi_h\omega_h\dot{h}(t)-\omega_h^2 h(t)\text{, (3)}$$

where

$$\omega_h=\sqrt{\frac{k_h}{m}}=2\pi f_h\text{, (4)}$$

$$\xi_h=\frac{c_h}{2\sqrt{k_h m}}\text{, (5)}$$

where ω_h, f_h, and ξ_h denote the natural circular frequency, the natural frequency, and the damping ratio of vertical bending, respectively. The velocity $\dot{h}(t)$ and displacement $h(t)$ can be obtained by discretizing Eq. (2a):

$$\dot{h}(t+\Delta t)=\dot{h}(t)+\frac{\Delta t}{6}\times\left(K_1+2K_2+2K_3+K_4\right)\text{, (6)}$$

$$h(t+\Delta t)=h(t)+\Delta t\times\dot{h}(t)+\frac{(\Delta t)^2}{6}\times(K_1+K_2+K_3),\ (7)$$

where

$$K_1=\frac{F_L(t)}{m}-2\xi_h\omega_h\dot{h}(t)-\omega_h^2h(t),\ (8a)$$

$$K_2=\frac{F_L(t)}{m}-2\xi_h\omega_h\left(\dot{h}(t)+\frac{\Delta t}{2}K_1\right)-\omega_h^2\left(h(t)+\frac{\Delta t}{2}\dot{h}(t)\right),\ (8b)$$

$$K_3=\frac{F_L(t)}{m}-2\xi_h\omega_h\left(\dot{h}(t)+\frac{\Delta t}{2}K_2\right)-\omega_h^2\left(h(t)+\frac{\Delta t}{2}\dot{h}(t)+\frac{(\Delta t)^2}{4}K_1\right),\ (8c)$$

$$K_4=\frac{F_L(t)}{m}-2\xi_h\omega_h\left(\dot{h}(t)+\frac{\Delta t}{2}K_3\right)-\omega_h^2\left(h(t)+\Delta t\cdot\dot{h}(t)+\frac{(\Delta t)^2}{2}K_2\right),\ (8d)$$

The discretized Eq. (6)~(7) can be solved with the initial conditions of $\dot{h}(t=0)=0$ and $h(t=0)=0$. The torsional motion Eq. (2b) for the section model can also be solved by the same method, which is omitted herein for brevity.

2.4 The fluid-structure coupling strategy

In the FSI analysis for aeroelastic problems, it is significant to satisfy the geometrical compatibility and the equilibrium conditions on the interface between the fluid and the structure (Zhang and Hisada, 2004). For this purpose, the strong coupling method or the weak coupling method has often been used to solve the FSI system. For the strong coupling method, sometimes referred to as directly coupling or simultaneous solution by some researchers, the variables of the coupled system is solved and corrected simultaneously. However, the use of strong coupling method is limited due to the less flexibility between the fluid and structure solver in the time integration. It also needs to modify the existing fluid dynamic solver and structure dynamic solver. Instead of directly solving the coupling system of Eq. (1) and (2), a weak coupling method is used to solve this fluid-structure coupling problem, by which the fluid and structural governing equations are sequentially solved and the interface conditions are satisfied in an iterative manner. Therefore, the existing solvers for fluid and structure can be easily adopted, and the flexibility between the fluid and structure solver is maintained. Furthermore, the weak coupling method requires less storage and computational time compared with the strong coupling method.

The flow chart of the computational process is shown in Fig. 4. Initially, the fully developed flow around the stationary deck section can be obtained. Meanwhile, the current flow condition provides the basis for the subsequent fluid-structure coupling simulation. At that moment, the corresponding lift force and torsional moment may be calculated by integrating the pressures and shear forces along the section surfaces. Then the calculated aerodynamic forces are employed as an input into the structural

motion solver to predict the displacement and velocity of the deck section. This velocity is then used to determine the new position at the next time-step. The *ANSYS FLUENT* re-meshes the computational domain in response to new geometry configuration. A series of aeroelastic problems can be efficiently simulated by this fluid-structure coupling strategy.

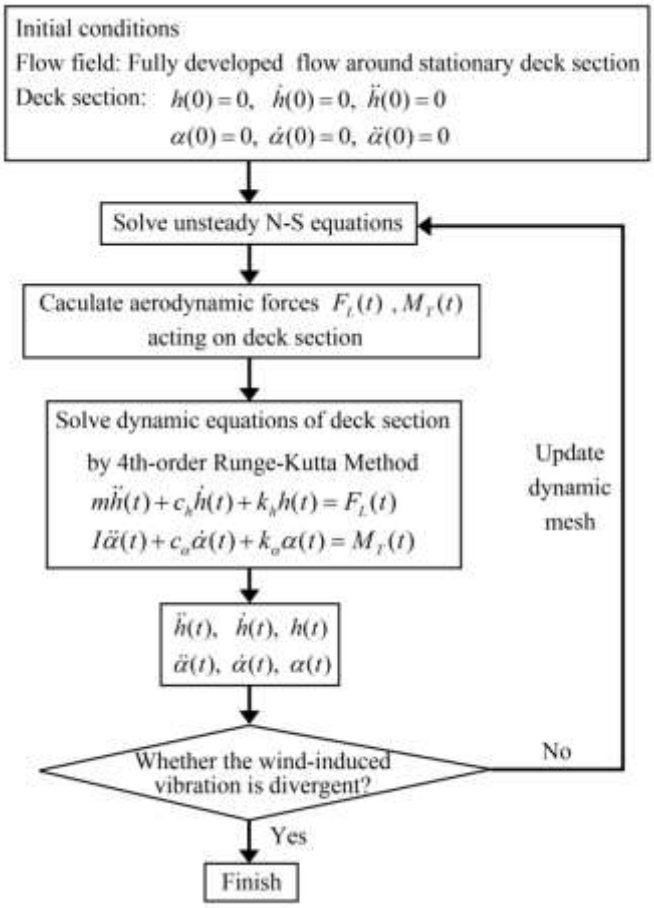

Fig. 4 Flow chart of the computational process

3. DESCRIPTION OF DECK SECTION AND SIMULATION CASES

Two representative sections are included in this study, and their scaled sections are depicted in Fig. 5. The first section is a thin flat plate, whose theoretical value of critical flutter speed is available, by which the validity and accuracy of the present numerical model can be verified. The second section originated from a streamlined cross-section of a steel box girder of the Taohuayu self-anchored suspension bridge (main span length: 406 m) in China. The aeroelastic tests for this deck section were conducted using the spring-supported section model in the wind tunnel laboratory by Long (2010). Table 1 shows the parameters of the section model in the wind tunnel tests. As shown by Long (2010), the soft flutter phenomenon was observed at the +5° initial attack angle for the section model without handrails.

At various initial angles of attack with different wind speed U_0, the wind-induced response of the deck model can be calculated by the numerical simulations, where the deck model is allowed to vibrate under the specified structural parameters as given in Table 1. The torsional and vertical responses (include displacement and velocity of the motion) are monitored to evaluate the vibrational performances of the deck section.

Fig. 5 Deck section of Taohuayu bridge (unit: mm)

Table 1 Parameters of the section model (Xu, 2006; Long, 2010).

Parameters	Symbols	Thin Plate	Bridge Deck
Width of the section model	B (m)	0.6	0.78
Height of the section model	H (m)	0.002	0.07
Mass of the section model	m (kg/m)	16.82	12.003
Mass moment of the section model	I (kg.m^2/m)	0.5856	0.4375
Natural frequency of vertical motion	f_h (Hz)	1.627	2.01
Natural frequency of torsional motion	f_α (Hz)	2.973	3.786
Damping ratio of vertical motion	ξ_h	0.006	0.005
Damping ratio of torsional motion	ξ_α	0.008	0.005

4. ANALYSIS OF DYNAMIC RESPONSE

4.1 Dynamic response of thin plate section

Fig. 6 shows the calculated time history of dynamic response for the thin plate section. The dynamic response of the thin plate almost decay to zero after initial perturbation at U_0 = 19.25 *m/s*, while the divergent vibration occurs at U_0 = 19.30 *m/s*. It indicates that the critical flutter speed of the thin plate is between 19.25~19.30 *m/s* according to the simulated results. The theoretical analysis results by Xu (2006) and the results from present simulations are compared in Table 2. The complex model method and the stochastic search method have the different judging criterion for determining the critical flutter state, result in the small deviations between the two sets of calculated results. Further details on these two methods can refer to Xu (2006). As can be seen, the numerically simulated critical flutter speed and frequency are in good agreement with the theoretical solutions, which verifies the accuracy of the present numerical model.

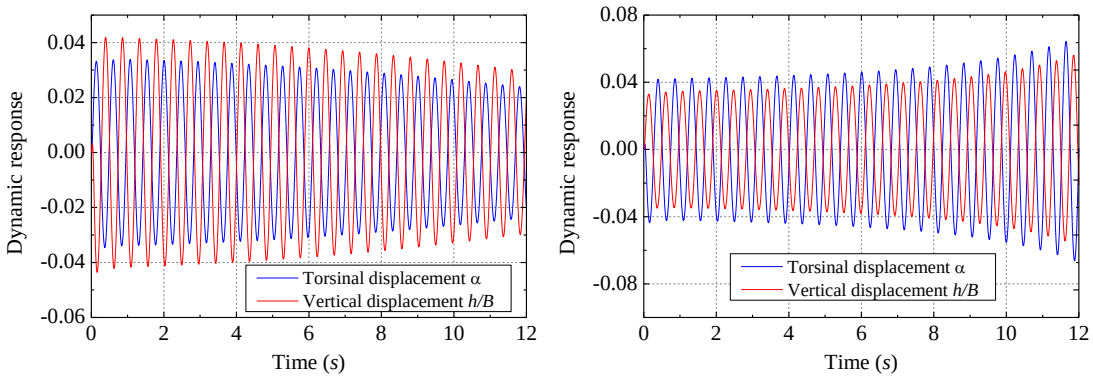

(a) U_0 = 19.25 *m/s*, *f*=2.145 *Hz* (b) U_0 = 19.3 *m/s*, *f*=2.143 *Hz*

Fig. 6 Time history of dynamic response, thin plate section

Table 2 Critical flutter wind speed and frequency of the thin plate

Calculation method		Critical flutter wind speed (*m/s*)	Flutter frequency (*Hz*)
Xu, 2006	Complex model method	19.35	2.165
	Stochastic search method	19.21	2.161
Present	Numerical simulation	19.25~19.30	2.143~2.145

4.2 Dynamic response of deck section

Fig. 7 shows the simulated time history of torsional and vertical displacements of the deck section at 5° attack angle under U_0 = 12 *m/s*. The torsional and vertical displacements increase gradually with flow time in the beginning, and then the motion changes from divergent vibration to steady-state vibration after about t=11*s*.

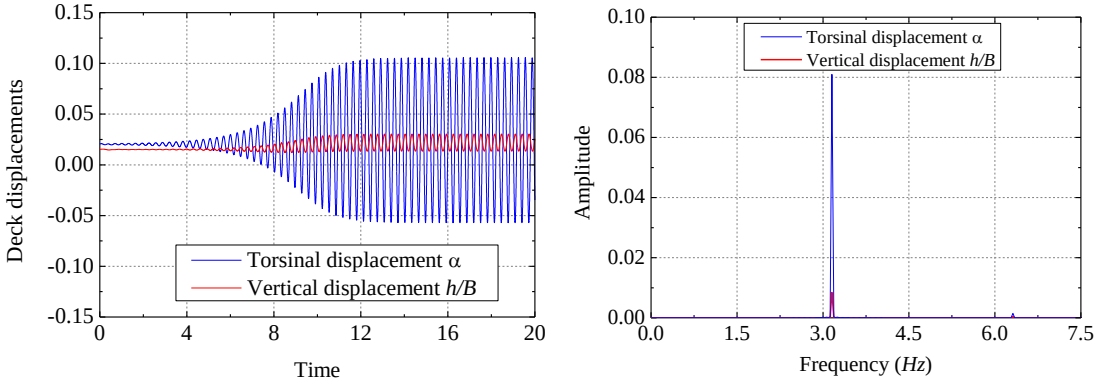

Fig. 7 Time history (left) and amplitude spectrum (right) of dynamic response, 5° initial attack angle, U_0 = 12 *m/s*

The unsteady flows around the elastically supported deck at different initial angles of attack are numerically simulated. Fig. 8 presents the calculated and experimental amplitudes of torsional and vertical displacement. The arrows in the figure show that any further increase in wind speed will result in divergent vibration and eventual hard flutter. The following observations can be made:

(1) For the case of 0° and +3° initial attack angle, no soft flutter phenomenon is observed, and the hard flutter occurs when the wind speed attains 15.2 *m/s* and 19.4 *m/s*, respectively.

(2) For the case of +5° initial attack angle, the soft flutter occurs when U_0≥11 *m/s* and the steady-state amplitude gradually increases with the wind speed. The divergent vibration (i.e., hard flutter) occurs when U_0＞13 *m/s*. Thus, the soft flutter can only occur at a certain range of wind speed. The sectional contour becomes much blunter with the increase of attack angle, leading to be more prone to soft flutter at large angle of attack.

Comparing with the experimental data, the torsional amplitudes are slightly overestimated while the critical wind speed of soft flutter appears to be underestimated. These discrepancies may be ascribed to the following causes: (a) the three-dimensional effects is captured in the experiments, while it's not considered in the numerical simulations; (b) the model geometry, the wall conditions and the elastically supported system inevitably have slightly differences between experimental tests and numerical simulations. The structural nonlinearity, the aerodynamic nonlinearity or both of them maybe responsible for LCO. It is impossible that the springs used in the wind tunnel tests are perfectly linear. However, in the numerical simulations, the bridge deck is idealized as a lumped mass, spring–dashpot system and the stiffness and damping of the deck model is set as constant. It means that the structural nonlinearity is not considered in the present simulations.

(3) The soft flutter occurs when U_0≥13.5 *m/s* for the case of -5° initial attack angle and the amplitude dramatically increases with the wind speed. The wind speed range of soft flutter for -5° attack angle is much narrower than that for +5° attack angle.

The numerically simulated results for the case of +5° initial attack angle will be focused on to further investigate the characteristics of soft flutter phenomenon.

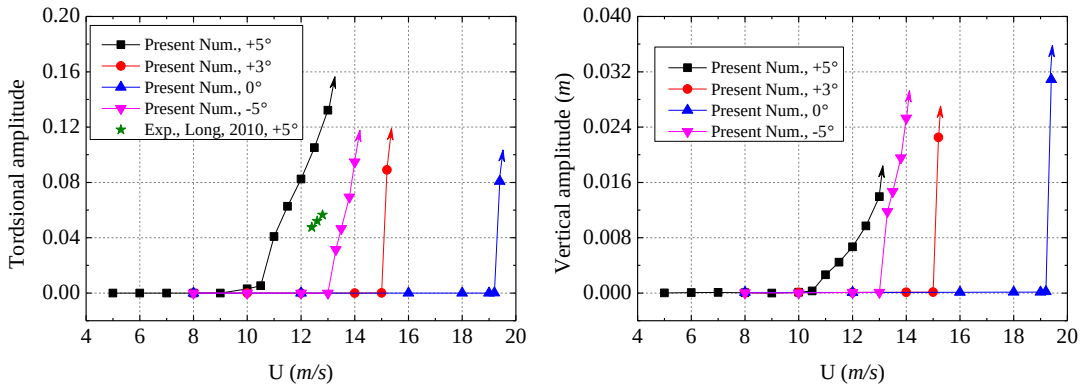

Fig. 8 Variation of dynamic response against wind speed

As can be seen in Fig. 7, the soft flutter of bridge deck is in a bending-torsion coupled mode, and the frequency of torsional and vertical motion is identical. Fig. 9 shows the

variation of coupled vibration frequency against the wind speed. The numerical simulation results are slightly smaller than those from wind tunnel test. The couple frequency almost linearly decreases with the increase of wind speed, and the causes of this phenomenon will be explained later. Furthermore, the structural damping has little effect on the frequency of soft flutter.

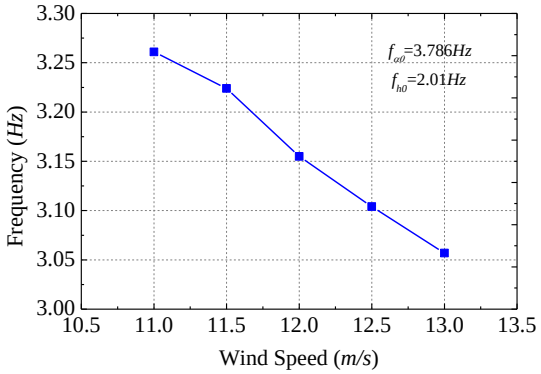

Fig. 9 Variation of motion frequency against wind speed

5. FLOW FIELD AROUND THE DECK SECTION

The pressure distribution on the surfaces of a deck section immersed in the fluid flow is generally represented by the dimensionless coefficient C_p, which is defined as:

$$C_p = \frac{P - P_{ref}}{1/2\,\rho U_0^{\,2}}, \quad (9)$$

where P_{ref} is reference pressure or environment pressure. The pressure distribution and flow field around the deck with structural damping ξ=0.005 at +5° initial attack angle will be analyzed in this section.

Fig.10 shows the diagrams of the instantaneous flow streamlines during one cycle of soft flutter at U_0 = 12.0 *m/s,* where 8 time instances are selected. The instantaneous pressure distribution at four different time instances is presented in Fig. 11. The following observations can be made:

(1) On the lower surface, no flow separation occurs for all the time instances selected. The pressure coefficients distributed on the lower surface almost remains unchanged during a motion cycle.

(2) At *t*=0 (snapshot 1), the deck attains the equilibrium position, and $\alpha(t=0)=1.39^{o}$. Large flow separation at the leading corner indicates large negative pressure at the windward side of upper surface, and following reattachment of flow towards the leeward side shows recovery of pressure. The extent of the separated bubble is about 1/3 of the deck width. This separated bubble can be called as the motion induced vortex (MIV).

(3) The situation for t=0 and t=0.25T (snapshot 2) are almost similar. The size of MIV increases with the increase of attack angle. The negative pressure at the leading edge of upper surface and positive pressure at the upwind side of inclined web maximize.

(4) From t=0.25T to t=0.5T, the flow separation intensifies and the size of the MIV increase with the decrease of attack angle. At t=0.5T, the separated flow reattaches to the trailing edge of upper surface, leading to a strong recovery of pressure. The pressure acting on the deck surface at wake region changes from negative to positive.

(5) From t=0.25T to t=0.75T, the deck section twirls from the maximum positive angle of attack to maximum negative one. The MIV moves to downstream with a velocity of about 25% of the free stream speed. At t=0.625T (snapshot 4), the flow is completely separated from the upper surface of deck section.

(6) In snapshots 5-6, the flow remains completely separated, which corresponding to no pressure recovery on the upper surface. The flow separation weakens with the decrease of attack angle. A new MIV is generated at the windward side of upper surface, and then the old MIV rapidly sheds from the deck section.

(7) The length of newly generated MIV is about 1/2 of the deck width (snapshot 7). From snapshot 7 to snapshot 8, the size of this MIV slightly decreases with the rotation of deck section in clockwise direction.

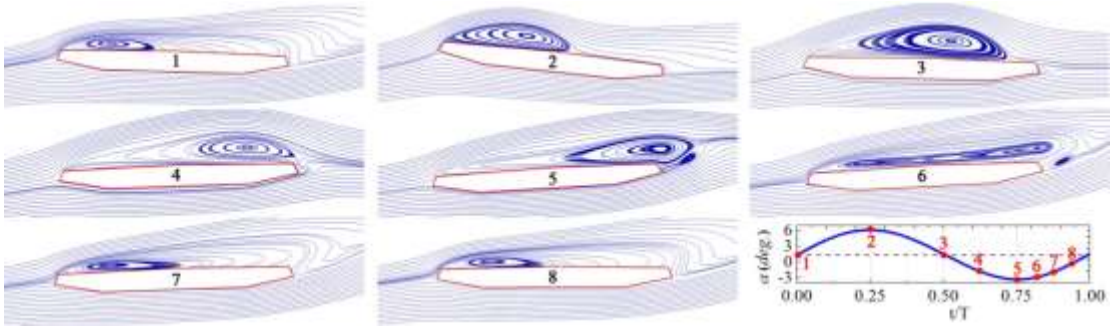

Fig. 10 Instantaneous flow streamlines plot, U_0 = 12.0 *m/s*

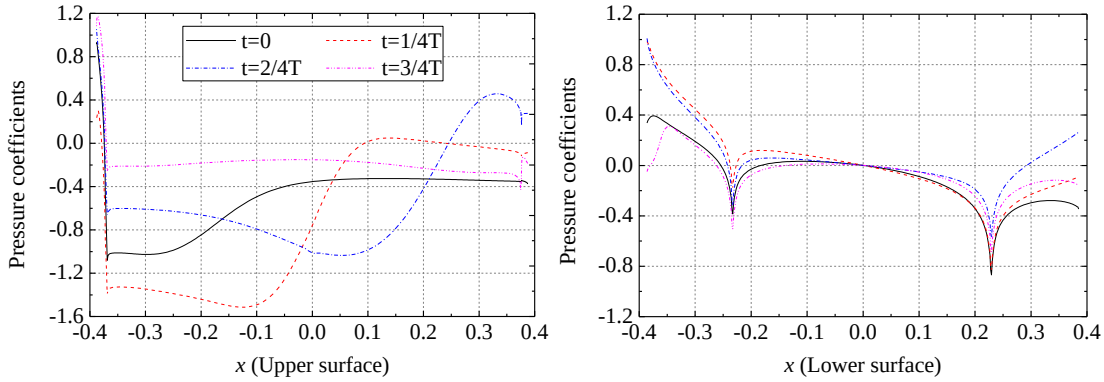

Fig. 11 Distribution of instantaneous pressure coefficients

According to the general knowledge of fluid dynamics, as the wind speed increases，the MIV moves faster, and may results in the increase of motion frequency. However, as shown in Fig. 9, the soft flutter frequency decreases with the increase of wind speed. One possible reason can be demonstrated as follows: taking the cases of 11 *m/s* and 13 *m/s* as the example. Fig. 12 shows the instantaneous flow streamlines when the deck section moves to the maximum positive angle of attack under two different wind speeds. The torsional amplitude increases and the flow separation intensifies with the wind speed. As a consequence, a much stronger MIV is generated at the leading edge of upper surface at a higher wind speed. It is interesting to observe that the MIV width significantly decreases with the increase of torsional amplitude. So the MIV takes a longer time to travel to the tailing edge and shed from the upper surface, leading to a longer period for soft flutter. In addition, for large-amplitude nonlinear vibrations, the period tends to be prolonged by larger amplitude.

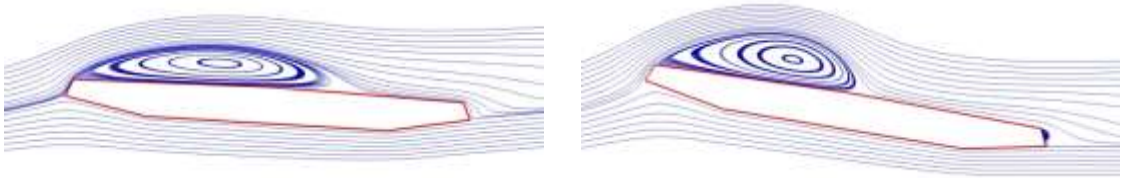

(a) U_0 = 11.0 *m/s* (b) U_0 = 13.0 m/s

Fig. 12 Instantaneous flow streamlines plot

6. PRELIMINARY DISCUSSION OF SOFT FLUTTER MECHANISM

From the point of view of energy, the steady response illustrates the energy balance must be hold between the input and output. Although the soft flutter of bridge deck is in a bending-torsion coupled mode, the dynamic response is dominated by torsion as shown in Fig. 11. The work done by twist moment can be expressed as

$$W_\alpha = \int_{t_1}^{t_2} M_T \dot{\alpha} dt \text{ , (10)}$$

Fig. 13 shows the time history of self-excited moment M_T, torsional displacement α and associated aerodynamic power $M_T\dot{\alpha}$ of the deck section during one soft flutter cycle.

The analysis of Section 4.6 shows that the MIV generated and shed periodically on the deck surface may be the fundamental cause of the soft flutter of the bridge deck. At the beginning of the vibration cycle, a large MIV is generated at the leading corner of leeward surface, which induces a strong nose-up (positive) moment. The MIV increases its strength, and the MIV-induced moment is so strong that it forces the deck section to rotate to a positive angle. The self-excited moment and the torsional motion are in the same direction at first quarter cycle, which results in $W_\alpha > 0$ as shown in Fig. 13. At t=1/4T~1/2T, the self-excited moment and the torsional velocity are in opposite

directions, thus $W_\alpha<0$. After *t*=1/2*T*, the MIV increases its strength as it moves to downstream. As the MIV travels to the trailing edge of upper surface, it generates a strong nose-down (negative) moment and results in a strong restoring impulse. At *t*=1/2*T*~3/4*T*, the deck section is forced to rotate to a negative angle as the flow time goes on, and the self-excited moment does positive work during this process. Then, the deck section moves back to the equilibrium position at *t*=3/4*T*~*T*, and $W_\alpha<0$ is also because the deck rotates in the opposite direction of twist moment. In a sense, the MIV also plays an intermediary role for the energy transfer between the structure and the wind flow. For the deck section at +5° attack angle, as mentioned above, the same soft flutter state is reached both from the rest and from the large initial perturbation. It indicates that the MIV can be generated spontaneously or by the initial perturbation.

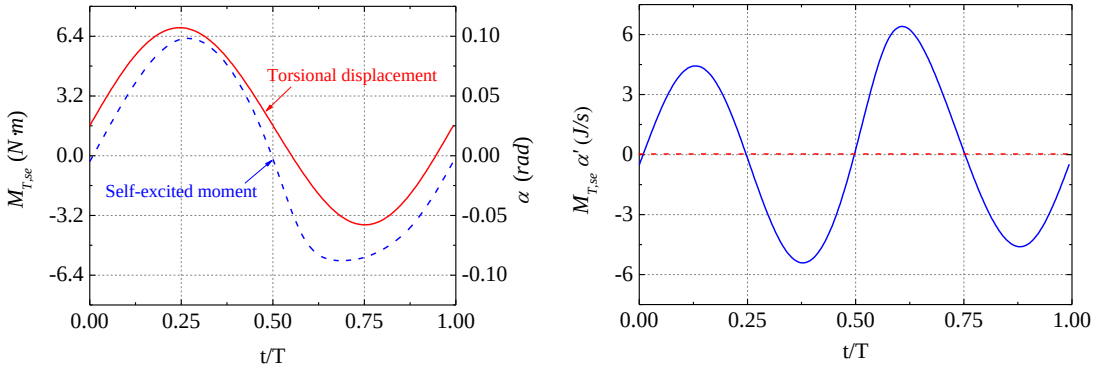

Fig. 13. Time history of aerodynamic moment, torsional displacement and associated aerodynamic power during one flutter cycle, 5° initial attack angle, U_0 = 12 *m/s*

Below the critical wind speed of soft flutter, the MIV caused by the initial perturbation is not strong enough to preserve the motion and the deck section is characterized by attenuated vibration. At the wind speed range of soft flutter, the MIV is strong enough when it moves along the surface of the deck section to generate large aerodynamic forces. The dynamic response of the deck section develops into steady state vibration due the strong nonlinearity of MIV-induced forces. As the wind speed increases, the strength of MIV becomes higher. After the critical wind speed of hard flutter, the energy absorbed from the wind flow through the MIV is more than that dissipated by structural damping, results in the occurrence of hard flutter.

7. CONCLUSIONS

Based on *ANSYS FLUENT*, a fluid-structure interaction (FSI) model has been developed to investigate the soft flutter characteristics of a bridge deck. The accuracy of present numerical model is verified by one thin plate section with theoretical solutions. The present numerical model successfully recaptures the soft flutter phenomenon of the bridge deck. With the increase of attack angle, the deck section becomes much blunter, and it is more prone to soft flutter. The soft flutter amplitude increases gradually with the wind speed until the hard flutter occurs.

The soft flutter of bridge deck is in a bending-torsion coupled mode, and the coupled vibration frequency linearly decreases with the increase of wind speed. The motion induced vortex (MIV) generated and shed periodically on the deck surface is the fundamental cause of the soft flutter of bridge deck. A stronger MIV is generated at the leading edge of deck surface, and the width of the MIV significantly decreases with the increase of torsional amplitude. So the MIV takes a longer time to travel to the tailing edge and shed from the deck surface, leading to a longer period for soft flutter. There must exist an aerodynamic energy balance for bridge deck during soft flutter, i.e., the fluid-structure system absorbs and dissipates energy in a certain vibration region so as to achieve the balance.

ACKNOWLEDGEMENTS

The research is jointly supported by the National Science Foundation of China (51178086, 51478087).

REFERENCES

Amandolese, X., Michelin, S., Choquel, M., 2013. "Low speed flutter and limit cycle oscillations of a two-degree-of-freedom flat plate in a wind tunnel." *Journal of Fluids & Structures*, **43**(6):244-255.

Chen, Z., Yu, X., Yang, G., and Spencer Jr, B., 2005. "Wind-induced self-excited loads on bridges." J*ournal of Structural Engineering*, **131**(12), 1783-1793.

Cunningham, A.M., 2003. "Buzz, buffet, and LCO on military aircraft: the aeroelastician nightmare." In: *Proc. International Forum on Structural Dynamics and Aeroelasticity*, Amsterdam.

Fransos, D., and Bruno, L. (2006). "Determination of the aeroelastic transfer functions for streamlined bodies by means of a Navier–Stokes solver." *Mathematical and Computer Modelling*, **43**(5), 506-529.

Hassan, M., Gerber, A., and Omar, H., 2010. "Numerical estimation of fluidelastic instability in tube arrays." *Journal of Pressure Vessel Technology*, **132**(4), 041307.

Long, F., 2010. "Wind-resistant performance analysis and experimental investigation on long-span self-anchored suspension bridge." Dalian University of Technology, China. (in Chinese)

Majid, D.L.A.H.A., Basri, S.N., 2008. "LCO flutter of cantilevered woven glass/epoxy laminate in subsonic flow." *Acta Mechanica Sinica*, **24**(1):107-110.

Menter, F. R., 1994. "Two-equation eddy-viscosity turbulence models for engineering applications." *AIAA Journal*, **32**(8):1598-1605.

Nomura, T., Hughes, T.J.R. (1992). "An arbitrary Lagrangian-Eulerian finite rigid element method for interaction of fluid and a rigid body." *Computer Methods in Applied Mechanics & Engineering*, **95**(1): 115-138.

Scanlan, R. H., and Tomo, J., 1971. "Air foil and bridge deck flutter derivatives." *Journal of Engineering Mechanics*, **97**(6), 1717-1737.

Schneider, G., and Raw, M. (1987). "Control volume finite-element method for heat transfer and fluid flow using colocated variables—1. computational procedure." *Numerical Heat Transfer, Part A Applications,* **11**(4), 363-390.

Tang, L., Bartels, R.E., Chen, P.C., et al., 2003. "Numerical investigation of transonic limit cycle oscillations of a two-dimensional supercritical wing." *J Fluid Struct*, **17**(1): 29-41.

Wang, B., Zha, G.C., 2011. "Detached-eddy simulation of transonic limit cycle oscillations using high order schemes." *Computers & Fluids*, **52**(52):58-68.

Xu, F.Y. (2005). "Identification of flutter derivatives and flutter analysis of bridge." Tongji University, China. (in Chinese)

Xu, F.Y., Chen, A.R., 2008. "3-D flutter analysis of Sutong bridge." *Engineering Mechanics*, **25**(8): 139-144. (in Chinese)

Xu, F. Y., Ying, X. Y., Zhang, Z. (2014). "Three-degree-of-freedom coupled numerical technique for extracting 18 aerodynamic derivatives of Bridge Decks." *Journal of Structural Engineering*, **140**(11).

Ying, X.Y., Xu, F.Y., Zhang, Z. (2012). "Numerical simulation and visualization of flow around rectangular bluff bodies." *Proc., BBAA 7 Int. Colloquium on Bluff Bodies Aerodynamics and Applications*, Shanghai, China.

Zhang, C.G., 2007. "Soft flutter and parameters identification of nonlinear self-excited aerodynamic force of bridge girder." Tongji University, China.

Zhang, Q. and Hisada, T. (2004). "Studies of the strong coupling and weak coupling methods in FSI analysis." *International Journal for Numerical Methods in Engineering*, **60**(12): 2013-2029.

Zhu, L., Gao, G., 2015. "Influential factors of soft flutter phenomenon for typical bridge deck sections."*Journal of Tongji University (Nautual Science)*, **43**(9): 1219-1294. (in Chinese)